1991

J. Molenaar

Multigrid for semiconductor device simulation:
cell-centered of vertex-centered multigrid ?

Department of Numerical Mathematics Report NM-R9118 December

CWI, nationaal instituut voor onderzoek op het gebied van wiskunde en informatica

CWI is the research institute of the Stichting Mathematisch Centrum, which was founded on February 11, 1946, as a non-profit institution aiming at the promotion of mathematics, computer science, and their applications. It is sponsored by the Dutch Government through the Netherlands organization for scientific research (NWO).

Multigrid for Semiconductor Device Simulation: Cell-centered or Vertex-centered Multigrid ?

J. Molenaar
Centre for Mathematics and Computer Science
P.O. Box 4079, 1009 AB Amsterdam, The Netherlands

We study the primal and dual mixed finite element discretization on rectangular grids for the semiconductor device equations. When suitable quadrature rules are used, the primal version is equivalent to the usual vertex-centered box scheme, whereas the dual version leads to a cell-centered finite volume discretization. In both cases the system of nonlinear equations obtained after discretization is solved by multigrid; we use cell-centered multigrid for the cell-centered scheme and vertex-centered multigrid for the vertex-centered scheme. In cell-centered multigrid it is necessary to apply a local damping of the restricted residual in order to deal with the strong nonlinearity of the problem. This can be avoided by using the vertex-centered multigrid algorithm provided that injection is used for the restriction of the residual. As is well known injection is usually too inaccurate a grid transfer operator for second order differential equations, but by means of a two-grid analysis we show that the choice of a suitable smoothing operator can alleviate this problem. In numerical experiments vertex-centered multigrid appears to be more efficient and robust for solving semiconductor equations than cell-centered multigrid.

1980 Mathematics Subject Classification: 65H10, 65N30, 65N50.
Keywords and Phrases: Semiconductor equations, mixed finite element method, multigrid methods.

1. Introduction

The electric behavior of semiconductor devices is usually described by the classical drift-diffusion model, that consists of a system of three nonlinear partial differential equations. In this paper we only consider the steady state equations in two space dimensions. The usual approach for the discretization of these equations is the application of a box method (finite volume method), where the fluxes between the control volumes are approximated by the one-dimensional Scharfetter-Gummel scheme (cf. [1, 16]). Brezzi et al. [3, 4] introduced a two-dimensional exponential fitting method for the semiconductor equations using a hybrid mixed finite element method. We consider both the primal and the dual version of the mixed finite element scheme on rectangular grids, and by using quadrature in the evaluation of the integrals involved we retain the classical Scharfetter-Gummel discretization of the fluxes; in fact, the dual version leads to a cell-centered finite volume scheme, whereas the primal version yields the usual box-scheme (vertex-centered finite volume scheme).

To solve the system of nonlinear equations obtained after discretization there are basically two approaches: either the equations are decoupled and solved iteratively (Gummel's iteration), or they are solved simultaneously. Gummel's iteration has the advantage that the linear systems involved are smaller and that it is more robust, i.e. it often converges even if a poor initial guess is available. Linear multigrid algorithms for solving the discretized continuity equations in Gummel's iteration have been proposed by Fuhrmann [7] and Reusken [19]. However, when the equations are strongly coupled Gummel's iteration converges slowly, so coupled approaches are more attractive. Usually the full system of equations is solved by Newton's method; the linear systems involved are either solved directly or their solution is approximated iteratively, e.g. by a preconditioned conjugate gradient method (cf. [16]). Nonlinear multigrid methods have also been proposed to solve the full system of equations. However, as the equations are strongly nonlinear, a priori it is not clear whether the coarse grid corrections really help. In the cell-centered multigrid methods in turns out to be necessary to apply a local damping of the restricted residual (cf. [15, 23]), due to fact that the corresponding

Report NM-R9118
ISSN 0169-0388
CWI
P.O. Box 4079, 1009 AB Amsterdam, The Netherlands

diagonal elements of the coarse and fine grid Jacobian matrices may differ by orders of magnitude; in vertex-centered multigrid methods (cf. [5]) this scaling problem does not seem to occur. Here we study both this scaling problem and the stability of the coarse grid operator. It is shown that the scaling problem can indeed be avoided by using a vertex-centered multigrid method with straight injection for the restriction of the residual. It is well known from Fourier analysis that injection is too inaccurate to be used in multigrid algorithms for solving second order differential equations: initial high frequency error modes are blown up in the coarse grid correction. Instead of using a more accurate restriction operator we construct a smoothing operator that effectively wipes out the 'dangerous' high frequency error modes. By a two-grid analysis we show that the use this smoothing operator leads to well-behaved two-grid algorithms indeed.

To compare the resulting cell-centered and vertex-centered multigrid algorithms in practice we consider two test-problems: a MOS-transistor and an LDDMOS-transistor. In numerical experiments it appears that vertex-centered multigrid is more efficient and robust than cell-centered multigrid.

An outline of this paper is as follows. In Section 2 we introduce the steady semiconductor equations, and in Section 3 we present the primal and dual mixed finite element discretizations. In Section 4 we discuss the scaling problems of the coarse and fine grid matrices, and the stability of the coarse grid operator. The two-grid analysis is carried out in Section 5 and in the next Section we present the results of our numerical experiments for both the cell-centered and the vertex-centered multigrid algorithm. In the last Section our conclusions are summarized.

2. The equations

The equations to be solved are

$$\begin{aligned} &\operatorname{div}\mathbf{j}_\psi = p - n + D, && \mathbf{j}_\psi = -\mu_\psi \operatorname{grad}\psi, \\ &\operatorname{div}\mathbf{j}_n = +R, && \mathbf{j}_n = +\mu_n(\operatorname{grad} n - n\operatorname{grad}\psi), \\ &\operatorname{div}\mathbf{j}_p = -R, && \mathbf{j}_p = -\mu_p(\operatorname{grad} p + p\operatorname{grad}\psi). \end{aligned} \tag{2.1}$$

Here the dependent variables are ψ, n and p, which denote the electrostatic potential and the concentrations of electrons and holes, respectively, and $\mathbf{j}_\psi$, $\mathbf{j}_n$ and $\mathbf{j}_p$, the displacement current and the current densities of electrons and holes, respectively. The first equation is Poisson's equation: μ_ψ is related to the dielectric constant and D is the (given) dope function. The other two equations are continuity equations for electrons and holes; μ_n and μ_p are the electron and hole mobilities, whereas R models the recombination rate of electrons and holes. For simplicity, in this paper we assume μ_n and μ_p to be constant.

In actual calculations we use the quasi-Fermi potentials ϕ_n and ϕ_p as the dependent variables; these are related to n and p by

$$\begin{aligned} n &= e^{\psi-\phi_n}, \\ p &= e^{\phi_p-\psi}. \end{aligned} \tag{2.2}$$

The set of equations (2.1) expressed in the variables (ψ, ϕ_n, ϕ_p) is strongly nonlinear, but the range of values assumed by (ψ, ϕ_n, ϕ_p) is of the same order of magnitude as the voltages applied to the device. This makes them better suited for numerical computation than e.g. (ψ, n, p) (cf. [16]).

In the discretization of the equations (2.1) we use the Slotboom variables (ψ, Φ_n, Φ_p),

$$\begin{aligned} \Phi_n &= e^{-\phi_n}, \\ \Phi_p &= e^{+\phi_p}, \end{aligned} \tag{2.3}$$

for which the equations appear in symmetric positive definite form:

$$
\begin{aligned}
-\operatorname{div}(\mu_\psi \operatorname{grad}\psi) &= e^{-\psi}\Phi_p - e^{+\psi}\Phi_n + D,\\
-\operatorname{div}(\mu_n e^{+\psi} \operatorname{grad}\Phi_n) &= -R,\\
-\operatorname{div}(\mu_p e^{-\psi} \operatorname{grad}\Phi_p) &= -R.
\end{aligned}
\tag{2.4}
$$

At the Ohmic contacts the boundary conditions are of Dirichlet type , (ψ, ϕ_n, ϕ_p) given , and at the outside boundaries we have homogeneous Neumann conditions: $\mathbf{n}\cdot\mathbf{j}_\psi = \mathbf{n}\cdot\mathbf{j}_n = \mathbf{n}\cdot\mathbf{j}_p = 0$, where $\mathbf{n}$ is the outward normal unit vector at the boundary. At silicon/oxide interfaces we have homogeneous Neumann boundary conditions for $\mathbf{j}_n$ and $\mathbf{j}_p$, while ψ and $\mathbf{j}_\psi \cdot \mathbf{n}$ are continuous, with $\mathbf{n}$ the normal unit vector at the interface (this means that we do not consider surface charges).

3. Mixed finite element discretizations

To derive a discretization of the set of equations (2.1) we decompose the standard second order elliptic problem with homogeneous boundary conditions into a system of first order equations:

$$\boldsymbol{\sigma} - A\operatorname{grad} u = 0, \qquad \text{on } \Omega, \tag{3.1a}$$

$$\operatorname{div}\boldsymbol{\sigma} = f, \qquad \text{on } \Omega, \tag{3.1b}$$

$$u = 0, \qquad \text{on } \delta\Omega_D, \tag{3.1c}$$

$$\mathbf{n}\cdot\boldsymbol{\sigma} = 0, \qquad \text{on } \delta\Omega_N, \tag{3.1d}$$

where $\delta\Omega_D$ and $\delta\Omega_N$ denote the parts of the boundary with Dirichlet or homogeneous Neumann boundary conditions, respectively. The sign is chosen such that $A > 0$.

First we introduce some notation. Let $L^2(\Omega)$ be the Hilbert space of square integrable functions on Ω with inner product $(\cdot,\cdot)$, let $H^{BC}(\operatorname{div}, \Omega)$ denote the Hilbert space of vector functions with Lebesgue integrable divergence,

$$H^{BC}(\operatorname{div}, \Omega) = \{\, \boldsymbol{\sigma} \mid \boldsymbol{\sigma} \in (L^2(\Omega))^2,\ \operatorname{div}\boldsymbol{\sigma} \in L^2(\Omega),\ \mathbf{n}\cdot\boldsymbol{\sigma} = 0 \text{ on } \delta\Omega_N\},$$

and let $H_0^1(\Omega)$ be the usual Sobolev space

$$H_0^1(\Omega) = \{\, u \mid D^\alpha u \in L^2(\Omega),\ 0 \leqslant |\alpha| \leqslant 1,\ u = 0 \text{ on } \delta\Omega_D\},$$

where D^α denotes the distributional derivative.

In the dual version of the mixed finite element method it is assumed that $\boldsymbol{\sigma}$ is a much smoother quantity than u because A can be a rapidly varying function, so one takes $\boldsymbol{\sigma} \in V = H^{BC}(\operatorname{div}, \Omega)$ and $u \in W = L^2(\Omega)$. We introduce the bilinear forms $a: V\times V \to \mathbb{R}$ and $b: V\times W \to \mathbb{R}$ by

$$a(\boldsymbol{\sigma}, \boldsymbol{\tau}) = \int_\Omega A^{-1}\boldsymbol{\sigma}\cdot\boldsymbol{\tau}\, d\Omega,$$

$$b(\boldsymbol{\sigma}, t) = \int_\Omega t \operatorname{div}\boldsymbol{\sigma}\, d\Omega,$$

and write (3.1) in its weak form: find $(\boldsymbol{\sigma}, u) \in V\times W$ such that

$$
\begin{aligned}
a(\boldsymbol{\sigma}, \boldsymbol{\tau}) + b(\boldsymbol{\tau}, u) &= 0, \qquad \forall \boldsymbol{\tau} \in V,\\
b(\boldsymbol{\sigma}, t) &= (f, t), \quad \forall t \in W,
\end{aligned}
\tag{3.2}
$$

with

$$(f, t) = \int_\Omega f t\, d\Omega.$$

However, in the primal version of the mixed finite element method we take $\boldsymbol{\sigma} \in \hat{V} = (L^2(\Omega))^2$ and $u \in \hat{W} = H_0^1(\Omega)$; the bilinear forms $\hat{a}: \hat{V}\times\hat{V} \to \mathbb{R}$ and $\hat{b}: \hat{V}\times\hat{W} \to \mathbb{R}$ are now defined by

$$\hat{a}(\boldsymbol{\sigma}, \boldsymbol{\tau}) = a(\boldsymbol{\sigma}, \boldsymbol{\tau}),$$

$$\hat{b}(\boldsymbol{\sigma}, t) = -\int_{\Omega} \boldsymbol{\sigma} \cdot \operatorname{grad} t \, d\Omega.$$

Again the equations (3.1) can be written in the form (3.2) but with a and b replaced by $\hat{a}$ and $\hat{b}$.

In the following we consider discretizations of both versions and assume that Ω can be divided by a regular partitioning in open disjoint, rectangular cells Ω^i, $\overline{\Omega} = \cup \overline{\Omega}^i$. To obtain the dual mixed finite element discretization we take the lowest order Raviart-Thomas elements [18] on the partitioned domain. Then, on each cell Ω^i we have its characteristic function e^i, and for each edge E^j, $E^j \not\subset \delta\Omega_N$, of a cell Ω^i we define the 'tent function' $\boldsymbol{\epsilon}^j$, i.e. the vector function of which each component is piecewise linear on all Ω^i and which satisfies $\boldsymbol{\epsilon}^j \cdot \mathbf{n}^k = \delta_{jk}$, where $\mathbf{n}^k$ denotes the unit vector normal on the edge E^j in the positive coordinate direction; δ_{jk} is the Kronecker delta. Our discrete approximation spaces are defined by

$$\begin{aligned} V_h &= \operatorname{span}(\boldsymbol{\epsilon}^j) \subset V, \\ W_h &= \operatorname{span}(e^i) \subset W. \end{aligned} \tag{3.3}$$

The dual mixed finite element discretization of (3.1) now formulates as follows: find $(\boldsymbol{\sigma}_h, u_h) \in V_h \times W_h$, such that

$$a(\boldsymbol{\sigma}_h, \boldsymbol{\tau}_h) + b(\boldsymbol{\tau}_h, u_h) = 0, \qquad \forall \boldsymbol{\tau}_h \in V_h, \tag{3.4a}$$

$$b(\boldsymbol{\sigma}_h, t_h) = (f, t_h), \qquad \forall t_h \in W_h. \tag{3.4b}$$

The integrals $b(\boldsymbol{\epsilon}_h^j, e_h^i)$ are easily evaluated; the integrals $a(\boldsymbol{\sigma}_h, \boldsymbol{\tau}_h)$ and (f, t_h) in (3.4) are approximated by a repeated, weighted trapezoidal rule for rectangles (cf. [17]):

$$\int_{\Omega} w(\mathbf{x}) z(\mathbf{x}) \, d\Omega = \sum_i \int_{\Omega^i} w(\mathbf{x}) z(\mathbf{x}) \, d\Omega \approx \sum_i \sum_{\nu=1,2,3,4} z(\mathbf{x}^{i,\nu}) \int_{\Omega^{i,\nu}} w(\mathbf{x}) \, d\Omega, \tag{3.5}$$

where $\mathbf{x}^{i,\nu}$ are the four vertices of Ω^i, and $\Omega^{i,\nu}$ the four quarter rectangles, parts of Ω^i, associated with these vertices, respectively.

If (f, t_h) is approximated by (3.5), with $w = t_h$ and $z = f$, we obtain from (3.4b)

$$\forall \Omega^i: \sum_j h^j d^{i,j} \sigma^j = \operatorname{area}(\Omega^i) \frac{1}{4} \sum_{\nu=1,2,3,4} f(\mathbf{x}^{i,\nu}), \tag{3.6}$$

with

$$d^{i,j} = \begin{cases} +1, & \text{if } E^j \text{ is a } n\text{- or } e\text{- edge of } \Omega^i, \\ -1, & \text{if } E^j \text{ is a } s\text{- or } w\text{- edge of } \Omega^i, \\ 0, & \text{otherwise,} \end{cases} \tag{3.7}$$

and h^j the length of edge E^j. We notice that (3.6) and (3.7) imply discrete current conservation.

For the approximation of $a(\boldsymbol{\sigma}_h, \boldsymbol{\tau}_h)$ we use (3.5) now with $w = A^{-1}$, and $z = \boldsymbol{\sigma}_h \cdot \boldsymbol{\tau}_h$. Here, the use of the trapezoidal rule can also be considered as lumping, because the matrix $a(\boldsymbol{\epsilon}^j, \boldsymbol{\epsilon}^k)$ is approximated by a matrix $\tilde{a}(\boldsymbol{\epsilon}^j, \boldsymbol{\epsilon}^k)$ that is diagonal:

$$\tilde{a}(\boldsymbol{\epsilon}^j, \boldsymbol{\epsilon}^k) = \delta_{jk} \int_{\Delta_E^k} A^{-1} \, d\Omega,$$

with $\Delta_E^k = \cup \{\Omega^{i,\nu} \mid \overline{\Omega}^{i,\nu} \cap E^k \neq \varnothing\}$; i.e. Δ_E^k is the dual box related with the edge E^k. If we consider the Poisson equation as an example of (3.1), with $A = 1$, then we see that it is advantageous to use lumping: after elimination of $\boldsymbol{\sigma}$ the non-lumped form of the discretization does not yield an M-matrix, whereas it is an M-matrix if lumping is used (cf. [17]). Moreover, for the continuity equations we retain the Scharfetter-Gummel scheme [20] by using the quadrature rule (3.5) (cf. [17]), with A^{-1} the exponentially varying function $A^{-1} = e^{\pm\psi}$. If we approximate ψ in Δ_E^k by a linear function, interpolating ψ from its values ψ^R and ψ^L in the neighboring cells Ω^i, $i = R, L$ we obtain

$$\int_{\Delta_E^k} e^{\psi}\, d\Omega = \text{area}\,(\Delta_E^k)\ \text{Bexp}^{-1}(\psi^R, \psi^L),$$

with

$$\text{Bexp}(x,\ y) = \frac{x - y}{e^x - e^y}.$$

For the discretization of the semiconductor equations (2.1) we apply the above scheme for the discretization of (3.1) to each of the three equations in (2.4); i.e. we apply the discretization procedure with $u = (\psi, \Phi_n, \Phi_p)$, $\boldsymbol{\sigma} = (\mathbf{j}_\psi, \mathbf{j}_n, \mathbf{j}_p)$ and $A = (-\mu_\psi, +\mu_n \exp(+\psi), -\mu_p \exp(-\psi))$, respectively. In order to obtain the usual definition of $(\mathbf{j}_\psi, \mathbf{j}_n, \mathbf{j}_p)$ (cf. [16]) we allow negative values for A. For an edge E^j with adjacent cells Ω^i, $i = R, L$, we obtain

$$\begin{aligned} j_\psi^j &= -\frac{h^j}{a^j}\mu_\psi(\psi^R - \psi^L), \\ j_n^j &= +\frac{h^j}{a^j}\mu_n \text{Bexp}(-\psi^R, -\psi^L)(\Phi_n^R - \Phi_n^L), \\ j_p^j &= -\frac{h^j}{a^j}\mu_p \text{Bexp}(+\psi^R, +\psi^L)(\Phi_p^R - \Phi_p^L), \end{aligned} \tag{3.8}$$

with h^j the length of E^j, and $a^j = \text{area}(\Delta_E^j)$. After elimination of the fluxes j^j we obtain a scheme that is equivalent to a finite volume scheme with control volumes Ω^i (see e.g. [16]) in the interior of the domain Ω. However, the geometry of this discretization is cell-centered as opposed to the usual box scheme that is vertex-centered. This has its influence mostly at the boundaries.

By using a suitable quadrature rule in the primal mixed finite element discretization we can obtain a scheme that is equivalent to the vertex-centered box-scheme (cf. [6]). On each vertex $\mathbf{x}^l$, $\mathbf{x}^l \notin \delta\Omega_D$, of some cell Ω^i we define the piecewise bilinear function $\hat{e}^l$ by $\hat{e}^l(\mathbf{x}^k) = \delta_{lk}$, and on each edge E^j we define the piecewise constant vector-valued function $\hat{\boldsymbol{\epsilon}}^j$, with $\hat{\boldsymbol{\epsilon}}^j$ parallel to E^j and $\|\hat{\boldsymbol{\epsilon}}^j\|$ the characteristic function on Δ_E^j.

Fully analogous to (3.3) and (3.4) our approximating subspaces are now defined by

$$\begin{aligned} \hat{V}_h &= \text{span}\,(\hat{\boldsymbol{\epsilon}}^j) \subset \hat{V}, \\ \hat{W}_h &= \text{span}\,(\hat{e}^i) \subset \hat{W}, \end{aligned} \tag{3.9}$$

and the primal mixed finite element discretization of (3.1) is: find $(\hat{\boldsymbol{\sigma}}_h, \hat{u}_h) \in \hat{V}_h \times \hat{W}_h$, such that

$$\hat{a}(\hat{\boldsymbol{\sigma}}_h, \hat{\boldsymbol{\tau}}_h) + \hat{b}(\hat{\boldsymbol{\tau}}_h, \hat{u}_h) = 0, \qquad \forall \hat{\boldsymbol{\tau}}_h \in \hat{V}_h, \tag{3.10a}$$

$$\hat{b}(\hat{\boldsymbol{\sigma}}_h, \hat{t}_h) = (f, \hat{t}_h), \qquad \forall \hat{t}_h \in \hat{W}_h. \tag{3.10b}$$

Following Fuhrmann [6] we introduce a quadrature rule for integrals over the dual boxes Δ_E^k: let $g \in C^0(\Delta_E^k)$ be a continuous function, then

$$\int_{\Delta_E^k} g\, d\Omega \approx \frac{\text{area}\,(\Delta_E^k)}{\text{length}\,(E^k)} \int_{E^k} g\, ds. \tag{3.11}$$

Direct application of (3.11) to the integrals in (3.10a), with u, $\boldsymbol{\sigma}$ and A as before, also yields the Scharfetter-Gummel discretization of the fluxes.

In order to interpretate (3.10b) as a conservation law we introduce dual boxes Δ_V^l that are related to the vertices $\mathbf{x}^l$ of cells: $\Delta_V^l = \cup\{\Omega^{i,\nu} \mid \mathbf{x}^l \in \overline{\Omega}^{i,\nu}\}$. By taking $\hat{t}_h = \hat{e}^l$ and using (3.11) we see that the left hand side of (3.10b) indeed equals the net influx in the dual cell Δ_V^l. If the right hand side of (3.10b) is also approximated by quadrature then

$$(f, \hat{e}^l) \approx f^l \int_\Omega \hat{e}^l\, d\Omega = f^l\ \text{area}(\Delta_V^l),$$

with $f^l = f(\mathbf{x}^l)$, we see that (3.10b) is the conservation law with respect to the dual box Δ_V^l, and we have regained a discretization that is equivalent to the usual vertex-centered box-scheme.

Finally, we discuss the treatment of the silicon/oxide interfaces, which we assume to be resolved by the edges E^j of the cells. In the primal mixed finite element discretization the continuity of ψ follows from the choice of $\hat{V}_h$, but the continuity of the displacement current $\mathbf{j}_\psi$ does not hold. In the dual version the continuity of ψ does not hold, whereas the continuity of the $\mathbf{j}_\psi$ in the direction normal to the interface is evident. For an edge E^j, with adjacent cells Ω^L and Ω^R that are in silicon and oxide region, we obtain from (3.4a) and (3.5) (cf. 3.8)

$$j_\psi^j = -\frac{2\mu_\psi^L \mu_\psi^R}{\mu_\psi^L a^R + \mu_\psi^R a^L} h^j (\psi^R - \psi^L),$$

i.e. we take the harmonic average of the coefficients μ_ψ.

4. Coarse grid correction

In this Section we study the coarse grid correction stage of multigrid algorithms for the two different discretizations of the semiconductor equations: the cell-centered scheme and the vertex-centered scheme. Due to the strong nonlinearity and bad scaling of the equations the construction of the coarse grid correction operator is not trivial at all. We focus our discussion on two points: the stability and the proper diagonal scaling of the coarse grid operator. The choice of a smoothing operator is discussed in Section 5.

For both mixed finite element discretizations that were derived in Section 3 we obtain the fine grids from the coarse grids by uniform refinement: starting from a coarsest grid finer grids are constructed by cell-wise refinement, i.e. the cells Ω_H^l on the coarse grid are split into 4 equal, smaller ones. This means that the cell-centered discretization gives rise to a cell-centered multigrid method (cf. Figure 4.1), whereas the vertex-centered discretization brings about a vertex-centered multigrid method (cf. Figure 4.2). The important difference between these two multigrid methods is that in vertex-centered multigrid the nodes of the coarse grid coincide with nodes on the fine grid, which is not the case in cell-centered multigrid.

The system of nonlinear equations on the fine grid can be written as

$$N_h(\bar{q}_h) = f_h. \tag{4.1}$$

The nonlinear coarse grid correction stage of a two-grid algorithm is then given by (cf. [2, 8])

$$N_H(\tilde{q}_H) = N_H(q_H) + \bar{R}_H(f_h - N_h(q_h)), \tag{4.2}$$

$$\tilde{q}_h = q_h + P_h(\tilde{q}_H) - P_h(q_H), \tag{4.3}$$

where N_H denotes the nonlinear coarse grid operator, P_h the (possibly nonlinear) prolongation operator for the solution, and $\bar{R}_H$ the restriction operator for the residual. As we only consider methods that treat the full system of equations, it seems impossible to construct the coarse grid operator N_H as the Galerkin approximation of N_h, so we construct N_H by discretization on the coarse grid. As the problem is nonlinear, this implies that the choice of the initial iterand on the coarse grid q_H determines the entries of the Jacobian matrix of the coarse grid operator.

There are several approaches for the selection of q_H. One can simply take the last available iterate in the full multigrid process, which is rather unsafe as q_H then depends on the history of the multigrid algorithm, so there is no guarantee that this iterate will remain in a neighborhood of the solution, and it may loose the properties that are required for a proper approximate solution. Other possibilities are to take $q_H = R_H q_h$, where R_H denotes a restriction operator for the solution, or to solve the problem on the coarse grid during the nested iteration, and to use that solution as initial iterate q_H each time the grid is visited in the multigrid iteration. Here we only consider the last two approaches.

A priori, it is not clear whether the problem on the coarse grid has a solution at all, or whether the coarse grid operator is stable. To get some insight in the last question we study the Jacobian matrices

$$J_H(\phi_H^i,\phi_H^l) = \frac{\partial(N_H(\phi_H))^i}{\partial\phi_H^l}, \qquad \phi = \psi, \phi_n, \phi_p, \tag{4.4}$$

that appear when Gummel's iteration is used to solve the coarse grid problem. For simplicity, we assume square grids and neglect the recombination rate R.

For Poisson's equation this matrix is always strongly diagonally dominant (cf. [16]). For the continuity equation for holes related to the cell Ω_H^C, with nearest neighbors Ω_H^N, $N = n,e,s,w$, we have

$$J_H(\phi_{p,H}^C,\phi_{p,H}^C) = +\mu_p e^{\phi_{p,H}^C - \psi_H^C} \sum_{N=n,e,s,w} B(\psi_H^N - \psi_H^C), \tag{4.5}$$

$$J_H(\phi_{p,H}^C,\phi_{p,H}^N) = -\mu_p e^{\phi_{p,H}^C - \psi_H^C} B(\psi_H^N - \psi_H^C) e^{\phi_{p,H}^N - \phi_{p,H}^C}, \tag{4.6}$$

with

$$B(x) = \frac{x}{e^x - 1},$$

the Bernoulli function. (The expression for the electron continuity equation is fully analogous.) It is known that the row sum of the Jacobian matrix for the hole continuity equation in Gummel's iteration is given by (cf. [11])

$$\sum_I J_H(\phi_{p,H}^C,\phi_{p,H}^I) = H(j_{p,H}^n + j_{p,H}^e - j_{p,H}^s - j_{p,H}^w),$$

the summation is over all cells Ω_H^I in the grid and H denotes the mesh size. This means that for the solution of the discrete problem on the coarse grid with zero right hand side ($R = 0$), the matrix is weakly diagonally dominant, if there is a Dirichlet boundary value available (cf. [22]).

If we construct the coarse grid solution as some restriction of the fine grid solution, it is not guaranteed that the coarse grid Jacobian matrix for the continuity equations is still weakly diagonal. In the following Theorem we estimate the row sum of the Jacobian matrix J_H that is scaled by the corresponding diagonal element .

THEOREM 4.1. *Let Ω_H^C be a cell with nearest neighbors Ω_H^N, $N = n,e,s,w$, then*

$$\frac{\sum_I J_H(\phi_{p,H}^C,\phi_{p,H}^I)}{J_H(\phi_{p,H}^C,\phi_{p,H}^C)} < 1$$

and

$$\left| \frac{\sum_I J_H(\phi_{p,H}^C,\phi_{p,H}^I)}{J_H(\phi_{p,H}^C,\phi_{p,H}^C)} \right| \leqslant \sum_{N=n,e,s,w} |1 - e^{\phi_{p,H}^N - \phi_{p,H}^C}|.$$

PROOF. Use $B(x) > 0$ and

$$\frac{\sum_I J_H(\phi_{p,H}^C,\phi_{p,H}^I)}{J_H(\phi_{p,H}^C,\phi_{p,H}^C)} = \frac{\sum_{N=n,e,s,w} B(\psi_H^N - \psi_H^C)(1 - e^{\phi_{p,H}^N - \phi_{p,H}^C})}{\sum_{N=n,e,s,w} B(\psi_H^N - \psi_H^C)}. \quad \square$$

Theorem 4.1 shows that if a restriction of the fine grid solution is used as initial iterate $q_H = q_H^R$ on the coarse grid, we may expect loss of diagonal dominance. However, if the solution of the coarse grid problem is fixed and used as initial iterate $q_H = q_H^F$ on the coarse grid, the matrices in Gummel iteration are all weakly diagonally dominant.

For the semiconductor equations (2.4) without any scaling, the residual of the continuity equations corresponds with the rate-of-change in the carrier concentrations. Without row scaling this means that the size of the residuals varies widely in magnitude throughout the domain. In the cell-centered

multigrid algorithm obtained from the dual mixed finite element discretization it may also happen that the diagonal elements of the Jacobian matrices for a father cell differ by orders of magnitude from the corresponding elements for the four kid cells, especially if the transition between n- and p-region is not properly resolved on the coarse grid. In this case a small residual (after row scaling) on the fine grid may result in a large correction on the coarse grid. Therefore it is necessary to apply a damping operator D_H for the restricted residual (cf. [15,23]). The modified coarse grid equation now reads

$$N_H(\tilde{q}_H) = N_H(q_H) + D_H \bar{R}_H(f_h - N_h(q_h)). \tag{4.7}$$

This D_H is a diagonal matrix with entries in [0, 1] that are determined by comparing the diagonal elements of the coarse and fine grid Jacobian matrices: for every cell Ω_H^I, which is split into four cells Ω_h^i, we have

$$D_H^I = \min \left[1, \frac{2|J_H(\phi_H^I, \phi_H^I)|}{\sup_{i=1,4} |J_h(\phi_h^i, \phi_h^i)|} \right], \qquad \phi = \psi, \phi_n, \phi_p. \tag{4.8}$$

In actual calculations we observe that damping is not necessary for Poisson's equation, and for the continuity equations the elements of D_H differ from 1 only in small parts of the domain (the transition regions), but there extremely small values ($< 10^{-10}$) for the diagonal elements appear. With this modified cell-centered multigrid algorithm good results were obtained for both one- and two-dimensional test problems (cf. [15,23]).

To understand the necessity of damping in cell-centered multigrid we consider the Jacobian matrix again. If a transition between n- and p-region is not properly resolved on the coarse grid, the hole concentration $e^{\phi_p^c - \psi^c}$, that appears in (4.5), explains the large variations in magnitude of $J(\phi_p^c, \phi_p^c)$ between coarse and fine grids in the cell-centered multigrid method. A possible solution for this problem is to construct q_H, by means of the L^2-projection of the variables (ψ, n, p); unfortunately, this choice may lead to ill-conditioning of the coarse grid matrix (see [13]).

This scaling problem can be avoided by using a vertex-centered multigrid method: if we use injection for the restriction of the solution, the electron and hole concentrations are equal in the coinciding coarse and grid fine points. In this case, if we assume a kind of monotonicity for ψ, we can prove that the corresponding elements of the Jacobian matrix are of the same order of magnitude on the coarse and fine grid.

THEOREM 4.2. *Let Ω_h^c be a cell of the fine grid with nearest neighbors Ω_h^l, $l = n,e,s,w$, and let Ω_H^C be the corresponding cell of the coarse grid, with nearest neighbors Ω_H^L, $L = N,E,S,W$ (see Figure 4.3). If vertex-centered multigrid is used, with injection for the restriction of the solution , and if, furthermore,*

$$\min_{l=n,e,s,w} \psi_h^l \leqslant \psi_h^c \leqslant \max_{l=n,e,s,w} \psi_h^l, \tag{4.9a}$$

and

$$\min(\psi_h^c, \psi_H^L) \leqslant \psi_h^l \leqslant \max(\psi_h^c, \psi_H^L), \tag{4.9b}$$

for $(l,L) = ((n,N),(e,E),(s,S),(w,W))$, then we have for the ratio of the corresponding diagonal elements of the fine and coarse grid Jacobian matrices

$$\frac{J_H(\phi_{p,H}^C, \phi_{p,H}^C)}{J_h(\phi_{p,h}^c, \phi_{p,h}^c)} \geqslant \frac{1}{4}.$$

PROOF. Suppose that $(\psi_h^l - \psi_h^c)$ is minimal for some $l = k$. From (4.9a) it follows that $\psi_h^k \leqslant \psi_h^c$, so from (4.9b) we conclude $\psi_H^K \leqslant \psi_h^k$. Using the fact that $B(x)$ is monotonically decreasing we obtain

$$\frac{J_H(\phi^C_{p,H},\phi^C_{p,H})}{J_h(\phi^c_{p,h},\phi^c_{p,h})} = \frac{\sum_{L=N,E,S,W} \mu_p e^{\phi^C_{p,H}-\psi^C_H} B(\psi^L_H - \psi^C_H)}{\sum_{l=n,e,s,w} \mu_p e^{\phi^c_{p,h}-\psi^c_h} B(\psi^l_h - \psi^c_h)}$$

$$= \frac{\sum_{L=N,E,S,W} B(\psi^L_H - \psi^C_H)}{\sum_{l=n,e,s,w} B(\psi^l_h - \psi^c_h)}$$

$$\geqslant \frac{B(\psi^K_H - \psi^C_H)}{4\,B(\psi^k_h - \psi^c_h)} \geqslant \frac{1}{4}. \quad \square$$

Theorem 4.2 shows that in a vertex-centered multigrid method local damping of the restricted residual is not necessary, provided that injection is used for the restriction of the residual $\bar{R}_H$. The use of e.g. full-weighting brings back the scaling problem. Moreover, if we assume that in vertex-centered multigrid the concentrations n and p on the coarse grid are a good point-wise approximation of the concentrations on the fine grid, we expect that the coarse grid operator, with q^F_H as initial iterate, is both stable and properly scaled.

This brings us to the point of the choice for the grid transfer operators P_h and $\bar{R}_H$. We have seen that in vertex-centered multigrid method it is attractive to use injection $\bar{R}^I_H$ for the restriction of the residual. For the prolongation of the solution in vertex-centered multigrid we define a nonlinear interpolation operator P^{NL}_h. For this interpolation, injection is used for the fine grid points, that also appear as coarse grid points (see Figure 4.2). Next we use the one-dimensional, current-conserving interpolation proposed by Hemker [9], to obtain values at the midpoints of the edges. Finally, we locally solve the equations at the middle of the cell, using the interpolated values at the midpoints of the edges as boundary conditions.

In the dual mixed finite elements discretization the approximating subspaces are nested, $V_H \subset V_h$ and $W_H \subset W_h$, so a natural set of grid transfer operators is available for the cell-centered multigrid algorithm (cf. [11, 15]). The prolongation P_h for the scalar quantities u_H is a piecewise constant interpolation, whereas the restriction of the residual is its transpose; these operators are denoted by P^C_h and $\bar{R}^C_H$, respectively. From (4.5) and (4.8) it follows that for $\bar{R}^C_H$ we have to apply the damping operator D_H in the cell-centered multigrid algorithm.

5. Two-grid analysis

In this Section we carry out a two-grid analysis for the cell-centered and the vertex-centered multigrid algorithms proposed in the previous Section. This is done because it is well known that the grid transfer operators proposed are too inaccurate to be used in multigrid algorithms for solving second order differential equations (cf. ([2, 10]). Our strategy to circumvent this possible source of problems is to take smoothing operators that can be used in combination with the inaccurate grid transfer operators, as we did before for Poisson's equation on a square grid (cf. [14]). For an introduction to two-grid Fourier analysis we refer to Stüben and Trottenberg [21].

We consider the anisotropic model problem

$$L\,u = -(A\frac{\partial^2}{\partial x^2} + \frac{\partial^2}{\partial y^2})\,u = f, \tag{5.1}$$

with $A > 0$, on the infinite domain $\Omega = \mathbb{R}^2$; this model problem can be considered as Poisson's equation on a rectangular, not necessarily square, grid. For both the cell-centered and the vertex-centered discretization the Fourier transform $\hat{L}_h : T_h \to \mathbb{C}$, $T_h = [-\pi,\pi)^2$, of the discretized operator L_h is given by

$$\hat{L}_h(\theta_x, \theta_y) = \frac{4}{h^2}(A\sin^2\frac{\theta_x}{2} + \sin^2\frac{\theta_y}{2}). \tag{5.2}$$

As usual in two-grid analysis we introduce a matrix notation for T_h: every $\boldsymbol{\theta} \in T_h$ is written as a 4-vector on T_H with entries $(\boldsymbol{\theta} + \pi\mathbf{p})$, where $\boldsymbol{\theta} \in T_H = [-\frac{\pi}{2}, \frac{\pi}{2})^2$ and $\mathbf{p} \in \{(0,0), (1,0), (0,1), (1,1)\}$. The accuracy of a restriction operator $\bar{R}_H$ is measured by the high frequency order m_H, i.e. the largest number m_H for which

$$\hat{\bar{R}}_H(\boldsymbol{\theta} + \pi\mathbf{p}) = \mathcal{O}(|\boldsymbol{\theta}|^{m_H}), \qquad \text{for } |\boldsymbol{\theta}| \to 0,\ \mathbf{p} \neq (0,0).$$

The high frequency order should at least be equal to the order of the differential equation being solved in order to avoid blow-up of high frequency error components in the coarse grid correction (cf. [2, 10]).

The two-grid error amplification matrix $M_h^{\nu_1,\nu_2}$ for a two-grid algorithm is defined by

$$M_h^{\nu_1,\nu_2} = S_h^{\nu_2}(I_h - P_h(L_H)^{-1}\bar{R}_H L_h) S_h^{\nu_1}, \tag{5.3}$$

where I_h denotes the identity operator and ν_1, ν_2 the number of pre- and post relaxation sweeps S_h, respectively. Using the techniques developed in [10, 14] we find for the cell-centered multigrid method, described in Section 4, that the Fourier transform $\hat{\mathbf{M}}_h^{0,0}$ in matrix representation of the coarse grid correction operator $M_h^{0,0}$ is given by

$$(\hat{\mathbf{M}}_h^{0,0})_{i,j} = \delta_{ij} - \frac{4 f_i f_j g_j}{A\sin^2\theta_x + \sin^2\theta_y}, \qquad i,j = 1, \cdots, 4, \tag{5.4a}$$

with

$$\begin{aligned}
f_1 &= \cos\frac{\theta_x}{2}\cos\frac{\theta_y}{2}, & g_1 &= A\sin^2\frac{\theta_x}{2} + \sin^2\frac{\theta_y}{2},\\
f_2 &= \sin\frac{\theta_x}{2}\cos\frac{\theta_y}{2}, & g_2 &= A\cos^2\frac{\theta_x}{2} + \sin^2\frac{\theta_y}{2},\\
f_3 &= \cos\frac{\theta_x}{2}\sin\frac{\theta_y}{2}, & g_3 &= A\sin^2\frac{\theta_x}{2} + \cos^2\frac{\theta_y}{2},\\
f_4 &= \sin\frac{\theta_x}{2}\sin\frac{\theta_y}{2}, & g_4 &= A\cos^2\frac{\theta_x}{2} + \cos^2\frac{\theta_y}{2}.
\end{aligned} \tag{5.4b}$$

From (5.4) we see that initial high frequency error modes in the neighborhood of $(0,\pi)$ and $(\pi,0)$ are blown up by the coarse grid correction, due to the inaccuracy of the restriction operator $\bar{R}_H$. The Fourier representation of $\bar{R}_H$ is

$$\hat{\bar{\mathbf{R}}}_H^C = \begin{bmatrix} f_1 & f_2 & f_3 & f_4 \end{bmatrix},$$

so its high frequency order m_H is only one, whereas it should be two.

The same problem occurs in vertex-centered multigrid when straight injection is used for the restriction and bilinear interpolation for the prolongation. In this case the coarse grid correction matrix is given by

$$(\hat{\mathbf{M}}_h^{0,0})_{i,j} = \delta_{ij} - \frac{4 \tilde{f}_i g_j}{A\sin^2\theta_x + \sin^2\theta_y}, \qquad i,j = 1, \cdots, 4, \tag{5.5a}$$

with

$$\begin{aligned}
\tilde{f}_1 &= \cos^2\frac{\theta_x}{2}\cos^2\frac{\theta_y}{2},\\
\tilde{f}_2 &= \sin^2\frac{\theta_x}{2}\cos^2\frac{\theta_y}{2},\\
\tilde{f}_3 &= \cos^2\frac{\theta_x}{2}\sin^2\frac{\theta_y}{2},\\
\tilde{f}_4 &= \sin^2\frac{\theta_x}{2}\sin^2\frac{\theta_y}{2},
\end{aligned} \tag{5.5b}$$

and g_j as in (5.4b). Now all initial high frequency error modes (θ_x,θ_y), with $\theta_x \to \pi$ or $\theta_y \to \pi$ are blown up by the coarse grid correction because the high frequency order m_H of $\bar{R}_H^f$ is zero.

The obvious remedy seems to be the use of more accurate restriction operators, but these have larger stencils which is undesirable for the semiconductor equations (see Section 4). Therefore we look for relaxation operators that effectively eliminate the dangerous high frequency error modes. Table 5.1 shows which of the high frequencies are eliminated by some standard smoothing operators for problem (5.1). For Poisson's equation discretized on a square grid ($A = 1$), we observe that point Gauss-Seidel can be used as the smoother in our cell-centered multigrid algorithm, as was found earlier in [14]. For the more general case ($A \neq 1$), we see that of the smoothers that do not mix frequencies only damped Jacobi relaxation, with damping parameter 0.5, eliminates one of the highest frequencies, viz. $(\theta_x,\theta_y) = (\pi,\pi)$. On the other hand red-black and zebra relaxation are more powerful smoothers, but they have the disadvantage of coupling frequencies; this is also shown in Table 5.1. Due to the coupling between high frequencies the alternating zebra relaxation, i.e. the combination of x-line zebra and y-line zebra relaxation, does not eliminate both the frequencies $(\pi,0)$ and $(0,\pi)$.

In order to eliminate all the highest frequencies we introduce the zebra-JOR relaxation S_h^{yJx} that consist of the sequence of a x-line zebra sweep, a damped Jacobi sweep (with damping factor 0.5) and a y-line zebra sweep. After the x-line zebra sweep and the JOR sweep both the high frequencies $(\pi,0)$ and (π,π) are eliminated; in the final y-line zebra sweep the high frequency $(0,\pi)$ is eliminated, while the two others are not reintroduced again. We notice that in the Jacobi sweep only half of the points need to be relaxed, as it follows the x-line zebra sweep.

As usual for relaxation operators that mix frequencies, we define the smoothing factor μ^{yJx} of zebra-JOR relaxation by

$$\mu^{yJx} = \sup_{\boldsymbol{\theta} \in T_H} \rho(\hat{\mathbf{Q}}\hat{\mathbf{S}}_h^{yJx}(\boldsymbol{\theta})),$$

where $\rho(\cdot)$ denotes the spectral radius, $\hat{\mathbf{S}}_h^{yJx}$ the Fourier transform of the iteration matrix of zebra-JOR relaxation and $\hat{\mathbf{Q}}$ the operator that annihilates all low frequencies

$$\hat{\mathbf{Q}} = \begin{bmatrix} 0 & & & \\ & 1 & & \\ & & 1 & \\ & & & 1 \end{bmatrix}.$$

Table 5.2 shows μ^{yJx} for different values of A; we conclude that zebra-JOR is a robust smoother.

As the last relaxation sweep of zebra-JOR is a zebra sweep, we can define a more accurate restriction operator $\bar{R}_H^Z$ for the vertex-centered multigrid algorithm, that also uses the residual from only one point, provided that in the last partial relaxation sweep of S_h^{yJx} (on the fine grid) the lines are relaxed that do not contain coarse grid points; its stencil is given by

$$\bar{R}_H^Z \simeq \frac{1}{8}\begin{bmatrix} 1 & 0 & 1 \\ 0 & 4 & 0 \\ 1 & 0 & 1 \end{bmatrix}. \tag{5.6}$$

The use of $\bar{R}_H^Z$ in combination with zebra relaxation is equivalent to the use of half weighting in combination with red-black relaxation (cf. [21]). The Fourier representation of $\bar{R}_H^Z$ is

$$\hat{\bar{\mathbf{R}}}_H^Z = \frac{1}{2}\begin{bmatrix} 1+\cos\theta_x\cos\theta_y & 1-\cos\theta_x\cos\theta_y & 1-\cos\theta_x\cos\theta_y & 1+\cos\theta_x\cos\theta_y \end{bmatrix},$$

so its high frequency order m_H is still 0, as with injection, but now there is no aliasing of the high frequencies $(\pi,0)$ and $(0,\pi)$ with $(0,0)$.

Besides the spectral radius $\rho(\cdot)$ of the error amplification matrix, we also study its spectral norm $\|\cdot\|_S$. The spectral norm $\|\hat{\mathbf{M}}_h^{\nu_1,\nu_2}\|_S$ of the two-grid error amplification matrix indicates what happens in a single two-grid cycle, whereas the spectral norm $\rho(\hat{\mathbf{M}}_h^{\nu_1,\nu_2})$ describes the convergence behavior after many cycles. We are interested in the supremum of these quantities with respect to $\boldsymbol{\theta}$ (the worst case behavior), so we define

$$\lambda_S^{\nu_1,\nu_2} = \sup_{\boldsymbol{\theta}\in T_H} \|\hat{\mathbf{M}}_h^{\nu_1,\nu_2}\|_S,$$

$$\lambda_\rho^{\nu} = \sup_{\boldsymbol{\theta}\in T_H} \rho(\hat{\mathbf{M}}_h^{\nu_1,\nu_2}),$$

with $\nu = \nu_1 + \nu_2$. Table 5.3 shows the $\lambda_S^{1,0}$ and λ_ρ^1 for three different multigrid algorithms: cell-centered multigrid, vertex-centered multigrid with straight injection $\bar{R}_H^I$ and vertex-centered multigrid with the more accurate restriction $\bar{R}_H^Z$. In all cases $\lambda_S^{1,0}$ is bounded so initial high frequency error modes are not blown up in a single two-grid cycle. The vertex-centered multigrid algorithm with straight injection $\bar{R}_H^I$ fails to converge in all cases ($\lambda_\rho^1 = 1$), whereas the use of $\bar{R}_H^Z$ yields an algorithm that does not converge for $A \gg 1$. The problem is that the low frequency (0,0) is not removed in the two-grid cycle, in fact we have

$$\lim_{|\boldsymbol{\theta}|\to 0} (\hat{\mathbf{M}}_h^{1,0})_{1,1} = \frac{-A^2}{(2+A)^2}.$$

When we interchange the x-zebra and the y-zebra sweep in the zebra-JOR relaxation, we get a two-grid algorithm that fails to converge for $A \ll 1$; in this case we have

$$\lim_{|\boldsymbol{\theta}|\to 0} (\hat{\mathbf{M}}_h^{1,0})_{1,1} = \frac{-1}{(1+2A)^2}.$$

Therefore we alternately use S_h^{xJy} and S_h^{yJx} in a series of two-grid cycles; the two-level convergence factor $\tilde{\lambda}_\rho^1$ for the two-grid cycle with a single relaxation sweep is now defined by

$$\tilde{\lambda}_\rho^1 = \left(\sup_{\boldsymbol{\theta}\in T_H} \rho(\hat{\mathbf{M}}_h^{0,0}\,\hat{\mathbf{S}}_h^{xJy}\,\hat{\mathbf{M}}_h^{0,0}\,\hat{\mathbf{S}}_h^{yJx})\right)^{\frac{1}{2}}.$$

The last column of Table 5.3 shows $\tilde{\lambda}_\rho^1$; the two-grid algorithm now converges for all values of A.

6. Numerical experiments

To compare the efficiency and the robustness of the multigrid algorithms that we have developed, we consider two test problems: a MOS-transistor and an LDDMOS-transistor.

In order to represent the geometry of these devices properly on the coarsest grid, we use non-uniform grids. The problem on the coarsest grid is solved by a combination of relaxation sweeps and Newton steps (cf. [9]). As it is necessary to use a relatively fine coarsest grid we use the HARWELL sparse matrix solver for the linear systems in Newton's method; it analyzes the sparsity pattern of the Jacobian matrix, which needs only be done once as we always use the same discretization method on all grids.

The continuation process to find a proper initial estimate is applied on the coarsest grid only. We start by solving the thermal equilibrium case (no applied voltages). Then we change the applied voltages and solve the problem on the coarsest grid using the previously obtained solution as initial

iterate; due to the robustness of the solution procedure we are able to take large steps. The coarse grid solution is interpolated to a next finer grid, and multigrid is used to solve the problem on the fine grid (nested iteration).

In our numerical experiments we consider both possibilities for constructing the coarse grid initial iterate q_H that are described in Section 4: either we 'freeze' the coarse grid solution q_H^F, or we use a restriction $q_H^R = R_H q_h$ of the fine grid solution. In vertex-centered multigrid we take injection for R_H, and in cell-centered multigrid we use the L^2-projection of the variables (ψ, ϕ_n, ϕ_p), which works successfully in the case of a bipolar transistor problem (cf. [13]). We only consider W-cycles, as it appeared that V-cycles are not sufficiently robust for the semiconductor problem (cf. [9, 15]). In all cases a single zebra-JOR sweep is used both for pre- and post smoothing; in vertex-centered multigrid the x-zebra and y-zebra sweeps are interchanged in the subsequent V-cycles that make up the W-cycle as indicated in Section 5. For details about the nonlinear relaxation operators we refer to [13, 15].

To estimate the convergence rate of the multigrid algorithms we introduce the average reduction factor ρ,

$$\rho = \left[\frac{d^{(10)}}{d^{(0)}} \right]^{\frac{1}{10}}, \tag{6.1}$$

where $d^{(i)}$ denotes the maximum of the scaled residual after i FAS-sweeps. The residual is scaled point-wise by means of the diagonal 3×3 blocks of the Jacobian matrix; thus the scaled residual corresponds with corrections that would occur in a point-wise collective Jacobi relaxation. The maximum of this scaled residual is taken over the grid and over the three variables (ψ, ϕ_n, ϕ_p).

Figure 6.1 gives a schematic view of the geometry and the doping profile of the MOS-transistor. The length of the device is 4.0 μm, the width is 1.5 μm and the oxide-layer is 0.05 μm thick. The recombination rate R is given by the Shockley-Read-Hall model,

$$R = \frac{np - 1}{\tau_p(n+1) + \tau_n(p+1)}, \tag{6.2}$$

where $\tau_n = \tau_p = 10^{-6}$ s are the electron and hole lifetimes, respectively. The applied voltages at the source, drain and substrate are kept constant at $V_{so} = 0.0\,\mathrm{V}$, $V_d = 0.1\,\mathrm{V}$ and $V_{su} = 0.0\,\mathrm{V}$, respectively. During the simulation the applied voltage at the gate is raised from $V_g = 0.0\,\mathrm{V}$ to $V_g = 5.0\,\mathrm{V}$ in steps of 1.0 V. Table 6.1 show the average residual factor ρ for the different multigrid algorithms on a 64×80 grid; the coarsest grid is an 8×10 grid, so 3 levels of uniform refinement are used. In all cases the multigrid algorithms converge rapidly; we observe that the vertex-centered algorithms are more efficient than the cell-centered multigrid algorithms.

A harder problem is the LDDMOS-transistor of which a plot is shown in Figure 6.2; a precise description of the device is found in the CURRY-example set [12]. We solve this problem only for the electrons, and assume that ϕ_p is piecewise constant; the recombination rate R is zero. We keep the applied voltages at the gate, substrate and source constant at $V_g = 2.0\,\mathrm{V}$, $V_{su} = 0.0\,\mathrm{V}$ and $V_{so} = 0.0\,\mathrm{V}$, respectively, while the drain voltage V_d is raised from 0.0 V to 5.0 V in steps of 1.0 V.

In this case the coarsest grid used is a 10×10 grid. Table 6.2 shows the average reduction factor ρ for the different multigrid algorithms. For this test problem the relaxation procedure sometimes fails on one of the coarse grids. In this case we do not use the correction calculated on that grid, and return to the finer grid immediately; in Table 6.2 these cases are indicated by an asterisk. Notice that only for vertex-centered multigrid with a frozen solution q_H^F on the coarse grids, we are able to use all grids: as shown in Section 4 in this case the coarse grid problems are properly scaled and stable. In Figure 6.3 we show the convergence behavior for much finer grids (the finest grid contains 320×320 cells) of this multigrid algorithm for $V_d = 5.0\,\mathrm{V}$; we observe that the convergence behavior is grid independent. Finally, we give a rough estimate for the execution times of the vertex-centered multigrid algorithm in Table 6.3; these results are obtained on a SUN SPARC station 1 for a non optimized PASCAL-code. As the convergence behavior is grid independent and the amount of work is proportional to the number of grid-points we conclude that multigrid has optimal complexity also for this

test problem.

7. Conclusions

We have derived two different mixed finite element discretizations of the stationary semiconductor equations, that are both equivalent to finite volume discretizations. To solve the systems of nonlinear equations obtained after discretization, we have developed a cell-centered and a vertex-centered multigrid algorithm. By studying the Jacobian matrices of the coarse grid problems it appears that the use of vertex-centered multigrid avoids the scaling problems that are inherent to the cell-centered multigrid method. Moreover, it is shown that the use of a restriction of the fine grid solutions as a starting solution on the coarse grid may lead to ill-conditioned coarse grid problems; it is better to calculate the solutions on the coarse grids during the nested iteration, and to use these solutions as starting iterate on the coarse grids during the multigrid iteration. In both cell-centered and vertex-centered multigrid we use inaccurate grid transfer operators for the restriction of the residual; by Fourier analysis it is shown that the choice of a suitable relaxation operator may lead to a well-behaved two-level algorithm for an anisotropic model problem. Our findings are confirmed by numerical experiments.

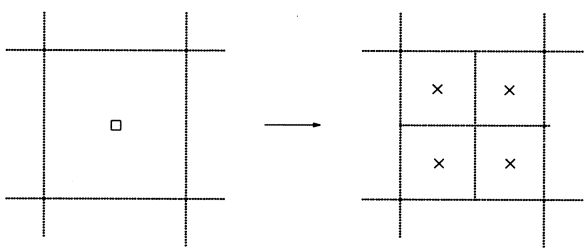

FIGURE 4.1. Coarse and fine grid nodes in cell-centered multigrid.

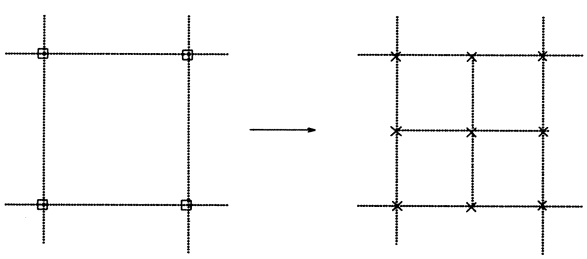

FIGURE 4.2. Coarse and fine grid nodes in vertex-centered multigrid.

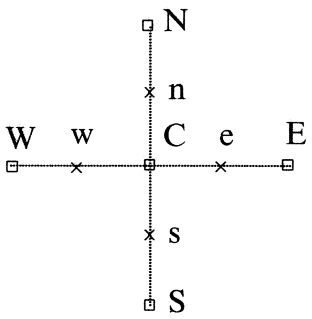

FIGURE 4.3. Numbering of nodes in vertex-centered multigrid.

Relaxation	$A = 1$	$A \neq 1$	Coupling
damped Jacobi (0.5)	(π,π)	(π,π)	-
point Gauss-Seidel	$(0,\pi)$, $(\pi,0)$	-	-
line Gauss-Seidel	-	-	-
red-black	$(\pi,0)$, $(0,\pi)$, (π,π)	(π,π)	$(\pi,0) \rightleftarrows (0,\pi)$
x-line zebra	$(\pi,0)$	$(\pi,0)$	$(\pi,\pi) \rightleftarrows (0,\pi)$
y-line zebra	$(0,\pi)$	$(0,\pi)$	$(\pi,\pi) \rightleftarrows (\pi,0)$

TABLE 5.1. Elimination and coupling of high frequency error modes for the model problem (5.1) by some standard smoothing operators.

A	μ^{yJx}
10^{-3}	0.125
10^{-2}	0.121
10^{-1}	0.095
10^{+0}	0.025
10^{+1}	0.095
10^{+2}	0.121
10^{+3}	0.125

TABLE 5.2. Smoothing factor μ^{yJx} of zebra-JOR relaxation for the model problem (5.1).

	Cell-centered MG		Vertex-centered MG				
	$\overline{R}_H$		$\overline{R}_H^I$		$\overline{R}_H^Z$		$\overline{R}_H^Z$
A	λ_ρ^1	$\lambda_S^{1,0}$	λ_ρ^1	$\lambda_S^{1,0}$	λ_ρ^1	$\lambda_S^{1,0}$	$\tilde{\lambda}_\rho^1$
10^{-3}	0.133	0.706	1.000	1.996	0.124	0.543	0.271
10^{-2}	0.144	0.693	1.000	1.962	0.116	0.534	0.260
10^{-1}	0.157	0.597	1.000	1.722	0.061	0.456	0.179
10^{+0}	0.202	0.357	1.000	1.423	0.111	0.212	0.111
10^{+1}	0.157	0.431	1.000	1.414	0.694	0.982	0.179
10^{+2}	0.144	0.490	1.000	1.414	0.961	1.359	0.260
10^{+3}	0.133	0.499	1.000	1.414	0.996	1.408	0.271

TABLE 5.3. Spectral norm $\lambda_S^{1,0}$ and radius λ_ρ^1 of the two-grid error amplification matrix with a single zebra-JOR pre-relaxation sweep.

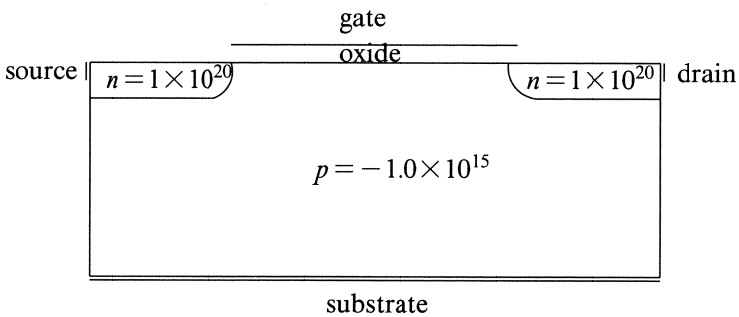

FIGURE 6.1. Geometry of MOS-transistor.

	q_H	0.0	1.0	2.0	3.0	4.0	5.0
Cell-centered MG	q_H^R	0.18	0.20	0.23	0.25	0.27	0.31
Cell-centered MG	q_H^F	0.19	0.20	0.35	0.37	0.40	0.41
Vertex-centered MG	q_H^R	0.15	0.15	0.17	0.17	0.16	0.16
Vertex-centered MG	q_H^F	0.16	0.16	0.16	0.15	0.16	0.19

TABLE 6.1. Average convergence factor ρ for different gate voltages V_g on 64×80 grid (MOS-transistor).

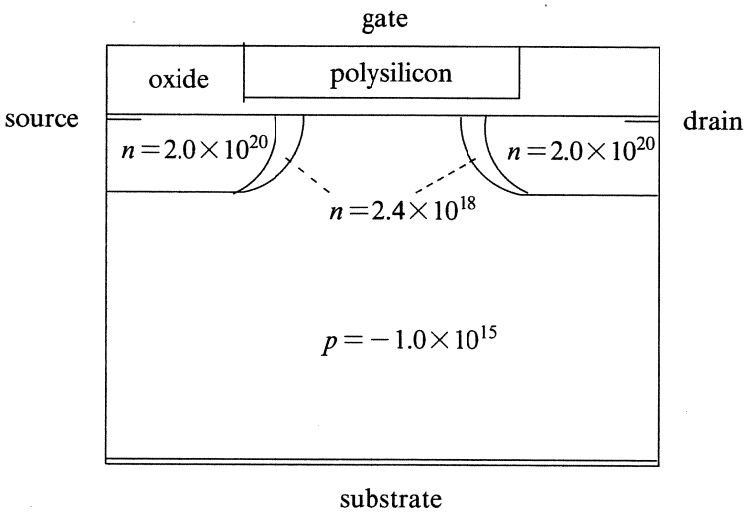

FIGURE 6.2. Geometry of LDDMOS-transistor.

	q_H	0.0	1.0	2.0	3.0	4.0	5.0
Cell-centered MG	q_H^R	0.20	0.52	0.63	0.74*	0.65*	0.74*
Cell-centered MG	q_H^F	0.23	0.47	0.44	0.74*	0.65*	0.74*
Vertex-centered MG	q_H^R	0.13	0.21	0.40*	0.80*	0.90*	0.91*
Vertex-centered MG	q_H^F	0.14	0.34	0.24	0.23	0.21	0.22

TABLE 6.2. Average convergence factor ρ for different drain voltages V_d on 80×80 grid (LDDMOS-transistor).

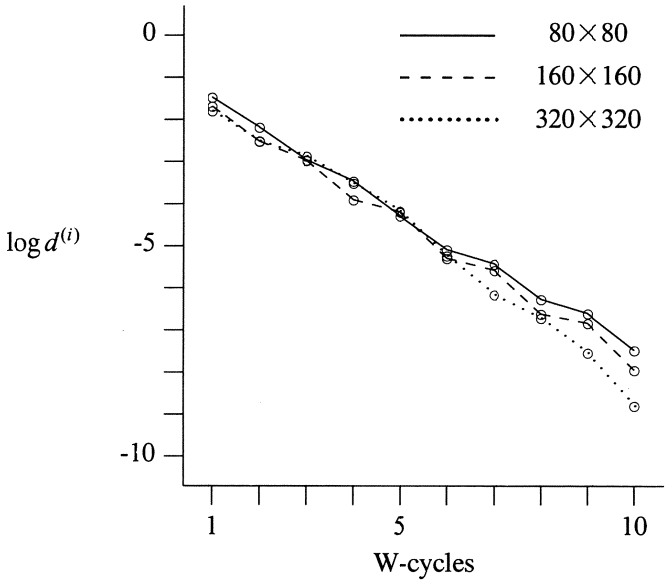

FIGURE 6.3. Convergence history of vertex-centered multigrid with $q_H = q_H^F$ for LDDMOS-transistor, $V_d = 5.0\,\mathrm{V}$.

grid	time in s
40×40	33
80×80	129
160×160	508
320×320	1959

TABLE 6.3. Estimation of time per W-cycle on a SPARC station 1.

REFERENCES

1. R.E. BANK, D.J. ROSE, and W. FICHTNER (1983). Semiconductor device simulation, *SIAM J.Sci.Stat.Comput.*, 4, 391-435.
2. A. BRANDT (1982). Guide to multigrid development, in *Multigrid Methods*, 220-312, ed. W. HACKBUSCH AND U. TROTTENBERG, Springer-Verlag, Lecture Notes in Mathematics 960.
3. F. BREZZI, L.D. MARINI, and P. PIETRA (1989). Numerical simulation of semiconductor devices, *Comp. Meths. Appl. Mech. and Engr.*, 75, 493-513.
4. F. BREZZI, L.D. MARINI, and P. PIETRA (1989). Two-dimensional exponential fitting and applications to drift-diffusion models, *SIAM J.Num.Anal.*, 26, 1342-1355.
5. R. CONSTAPEL and M. BERGER (1989). A Multigrid Approach for Device Simulation Using Local Linearization, in *Proceedings NASECODE VI*, 355-359, ed. J.J.H. MILLER, Boole Press Ltd., Dublin.

6. J. FUHRMANN (1990). An interpretation of the Scharfetter-Gummel scheme as a mixed finite element discretization, in *Fourth Multigrid Seminar*, 1-7, ed. G. TELSCHOW, Karl-Weierstrass-Institut fur Mathematik, Berlin.
7. J. FUHRMANN and K. GÄRTNER (1990). Incomplete factorization and linear multigrid algorithms for the semiconductor device equations, in *Proceedings IMACS conference*, Brusssels.
8. W. HACKBUSCH (1985). *Multigrid Methods and Applications*, Springer-Verlag, Berlin, Series in Computational Mathematics 4.
9. P.W. HEMKER (1990). A nonlinear multigrid method for one-dimensional semiconductor device simulation: results for the diode, *J.Comp.Appl.Math.*, 30, 117-126.
10. P.W. HEMKER (1990). On the order of prolongations and restrictions in multigrid procedures, *J.Appl.Math.*, 32, 423-429.
11. P.W. HEMKER and J. MOLENAAR (1991). An adaptive multigrid approach for the solution of the 2D semiconductor equations, in *International Series of Numerical Mathematics 98*, ed. W. HACKBUSCH AND U. TROTTENBERG, Birkhauser Verlag, Basel.
12. C. LEPOETER (1987). *CURRY example set,* Technical Report No. 4322.271.6005, Philips, Corp. CAD Centre, Eindhoven.
13. J. MOLENAAR (1991). *Adaptive multigrid applied to a bipolar transistor problem,* Report NM-R9115, Centre for Mathematics and Computer Science, Amsterdam.
14. J. MOLENAAR (1991). *A two-grid analysis of the combination of mixed finite elements and Vanka-type relaxation,* Report NM-R9102, Centre for Mathematics and Computer Science, Amsterdam.
15. J. MOLENAAR and P.W. HEMKER (1990). A multigrid approach for the solution of the 2D semiconductor equations, *IMPACT*, 2, 219-243.
16. S.J. POLAK, C. DEN HEIJER, W.H.A. SCHILDERS, and P. MARKOWICH (1987). Semiconductor device modelling from the numerical point of view, *Int.J.Num.Meth.Engng.*, 24, 763-838.
17. S.J. POLAK, W.H.A. SCHILDERS, and H.D. COUPERUS (1988). A finite element method with current conservation, in *Proc. SISDEP-88*, 453-462, ed. G. BACCARANI AND M. RUDAN, Bologna.
18. P.A. RAVIART and J.M. THOMAS (1977). A mixed finite element method for second order elliptic problems, in *Mathematical aspects of the finite element method*, Springer-Verlag, Lecture Notes in Mathematics 606.
19. A. REUSKEN (1991). Multigrid applied to two-dimensional exponential fitting for drift-diffusion models, in *Proceedings of the International Symposium on Iterative Methods in Linear Algebra*, Brusssels, To appear.
20. D.L. SCHARFETTER and H.K. GUMMEL (1969). Large-Signal Analysis of a Silicon Read Diode Oscillator, *IEEE Trans.E.D.*, ED-16, 64-77.
21. K. STÜBEN and U. TROTTENBERG (1982). Multigrid methods: fundamental algorithms, model problem analysis and applications, in *Multigrid Methods*, 220-312, ed. W. HACKBUSCH AND U. TROTTENBERG, Springer-Verlag, Lecture Notes in Mathematics 960.
22. D.M. YOUNG (1971). *Iterative solution of large linear systems*, Academic Press, New York.
23. P.M. DE ZEEUW (1991). Nonlinear multigrid applied to a 1D stationary semiconductor model, *SIAM J.Sci.Stat.Comput.*, To appear.